

# Gradient-Based Pulsed Excitation and Relaxation Encoding in Magnetic Particle Imaging

Guang Jia, Liyu Huang, Ze Wang, Xiaofeng Liang, Yu Zhang, Yifei Zhang, Qiguang Miao, Kai Hu, Tanping Li, Ying Wang, Li Xi, Xin Feng, Hui Hui, and Jie Tian, *Fellow, IEEE*

**Abstract**—Magnetic particle imaging (MPI) is a radiation-free vessel- and target-imaging modality that can sensitively detect nanoparticles. A static magnetic gradient field, referred to as a selection field, is required in MPI to provide a field-free region (FFR) for spatial encoding. The image resolution of MPI is closely related to the size of the FFR, which is determined by the selection field gradient amplitude. Because of the limitations of existing gradient coil hardware, the image resolution of MPI cannot satisfy the clinical requirements of human in vivo imaging. Pulsed excitation has been confirmed to improve the image resolution of MPI by breaking down the ‘relaxation wall.’ This work proposes the use of a pulsed waveform magnetic gradient from magnetic resonance imaging to further improve the image resolution of MPI. Through alignment of the gradient direction along the field-free line (FFL), each location on the FFL is able to have a unique excitation field strength that generates a specific relaxation-induced decay signal. Through excitation of nanoparticles on the FFL with many gradient profiles, a high-resolution, one-dimensional (1D) image can be reconstructed on the FFL. For larger magnetic nanoparticles, simulation results revealed that a pulsed excitation field with a greater flat portion generates a 1D bar pattern phantom image with a higher correlation and spatial resolution. With parallel FFL and gradient coil movements, high-resolution, two-dimensional (2D) Shepp–Logan phantom and brain vessel maps were reconstructed through repetition of the spatially resolved measurement of magnetic nanoparticles on the FFL.

**Index Terms**—Magnetic particle imaging, pulsed excitation, gradient field, field free line, spatial encoding, tomography, magnetic nanoparticles, Debye relaxation time, system matrix, singular value decomposition.

## I. INTRODUCTION

MAGNETIC particle imaging (MPI) is a novel imaging modality that sensitively detects superparamagnetic iron oxide particles without ionizing radiation [1]. The superior contrast and safety of MPI allow for blood vessel imaging, e.g., angiography [2], perfusion imaging [3], and functional neuroimaging [4]. The superior sensitivity of MPI allows for molecular target imaging, such as inflammatory plaque detection [5], stem cell tracking [6], and T cell tracking [7]. Magnetic hyperthermia with MPI guidance allows for a focused theranostic approach encompassing tumor treatment planning and monitoring [8].

However, the image resolutions of current MPI techniques are significantly limited by the selection field gradient amplitude. In MPI, a static magnetic gradient field, namely, selection field, is required to provide a field-free region (FFR) for spatial encoding [9]. An FFR can be a field-free point (FFP) or field-free line (FFL) [10], in which magnetic nanoparticles can be freely excited to generate signals [11]. Through steering of an FFL through the volume of interest [12], sufficient data in the Radon space can be collected [13]. Common projection reconstruction methods, such as filtered back-projection [14], can then be used to reconstruct the magnetic nanoparticle distribution image [15]. The MPI image resolution is directly related to the size of the FFP or the width of the FFL [14], which is determined by the selection field gradient amplitude [16]. Because of the limitations of existing gradient coil hardware, the image resolution of MPI cannot satisfy the clinical

This work was supported in part by the National Key Research and Development Program of China under Grant No: 2017YFA0700401, in part by the National Natural Science Foundation of China under Grant No: 62027901 and Grant No: 11974267, and in part by the 111 Project under Grant No. B17035. (Corresponding author: Guang Jia, Tanping Li, and Jie Tian.)

G. Jia, Z. Wang, X. Liang, Y. Zhang, Y. Zhang, and Q. Miao are with the School of Computer Science and Technology, Xidian University, Xi'an Shaanxi 710071, China (e-mail: gjia@xidian.edu.cn; 1245390633@qq.com; 15517326336@163.com; 892483869@qq.com; 1203154631@qq.com; qgmiao@xidian.edu.cn).

L. Huang is with the School of Life Science and Technology, Xidian University, Xi'an Shaanxi 710071, China (e-mail: huangly@mail.xidian.edu.cn).

K. Hu and T. Li are with the School of Physics, Xidian University, Xi'an Shaanxi 710071, China (e-mail: 1733721876@qq.com; tpli@xidian.edu.cn).

Y. Wang and L. Xi are with the School of Physical Science and Technology, Lanzhou University, Lanzhou, Gansu 730000, China (e-mail: yingw@lzu.edu.cn; xili@lzu.edu.cn).

X. Feng and H. Hui are with the CAS Key Laboratory of Molecular Imaging, Beijing Key Laboratory of Molecular Imaging, the State Key Laboratory of Management and Control for Complex Systems, Institute of Automation, Chinese Academy of Sciences, Beijing, 100190, China, and also with the School of Artificial Intelligence, University of Chinese Academy of Science, Beijing, 100080, China (e-mail: xin.feng@ia.ac.cn and hui.hui@ia.ac.cn).

J. Tian is with the CAS Key Laboratory of Molecular Imaging, Beijing Key Laboratory of Molecular Imaging, the State Key Laboratory of Management and Control for Complex Systems, Institute of Automation, Chinese Academy of Sciences, Beijing, 100190, China, and also with the Beijing Advanced Innovation Center for Big Data-Based Precision Medicine, School of Engineering Medicine, Beihang University, Beijing, 100083, China (e-mail: tian@ieee.org).

requirements of human in vivo imaging [17].

To improve the spatial resolution of MPI, a pulsed waveform magnetic field can be used to excite the magnetic nanoparticles. In conventional MPI, a continuous sinusoidal excitation field is typically used to induce a non-linear magnetization response in magnetic nanoparticles [18]. A high excitation field amplitude is required to generate a harmonic signal in the non-linear saturation region of the magnetization. However, this high excitation field is limited by human bio-safety concerns, such as magnetostimulation and specific absorption rate (SAR). Moreover, large nanoparticles exhibit a strong relaxation behavior under sinusoidal excitation, which induces significant lag and blurring of the signal [19]. To excite large nanoparticles with a significant relaxation effect, the use of low-amplitude pulsed waveform excitation was recently proposed [20]. Pulsed excitation leads to an exponential decay-like signal that can be modeled by Debye relaxation [21], which reduces signal blurring and improves the image resolution of MPI by breaking down the ‘relaxation wall’ [22].

This paper proposes the use of pulsed-waveform transverse magnetic gradients from magnetic resonance imaging (MRI) as an excitation field to further improve the image resolution of MPI. In MRI, protons at each gradient location have slightly different Larmor frequencies [23]. Slice selection, phase encoding, and frequency encoding can be performed through the activation of different direction gradients for short periods to accomplish Fourier-transform-based signal acquisition and image reconstruction [24]. Through alignment of the gradient direction along with the FFL, the nanoparticles on the FFL can be inhomogeneously excited with different pulsed-field amplitudes. Given that the relaxation time varies with the magnitude of the applied pulsed magnetic field [25], each location on the FFL has a unique excitation field strength that generates a specific relaxation-induced decay signal [20]. The received signal is the summation of the product of the signal from the unit concentration and the specific nanoparticle concentration at each FFL location. The collected signals can be combined for the system matrix-based one-dimensional (1D) image reconstruction of the FFL through the application of many pulsed excitation gradient profiles.

In this study, we evaluated the feasibility of a high-resolution tomographic imaging method using pulsed gradient field excitation. Toward this objective, we simulated the pulsed-gradient excitation process on an FFL for relaxation encoding. We also developed a system matrix-based reconstruction method for a 1D bar pattern phantom, two-dimensional (2D) Shepp–Logan phantom, and brain vessel maps. Finally, we evaluated the effect of the particle size and pulsed waveform on the reconstructed image quality.

## II. THEORY

In this section, we describe the theory of gradient-based pulsed excitation for relaxation encoding along with an FFL. We used the convention that the FFL is along the  $x$ -direction, and that the center of the field of view (FOV) is at the origin of the coordinate axes ( $x=y=z=0$ ). We assumed fully recovered

magnetization at the end of the flat portion during each pulse cycle; therefore, we did not consider steady-state establishment.

### A. Gradient-based Pulsed Excitation Field

We selected an MRI transverse gradient using a pair of Helmholtz coils as an inhomogeneous dynamic magnetic field to excite the nanoparticles. Both the magnetic field direction and gradient direction on the FFL were the same as the FFL direction. When activated, these gradient coils superimposed a linear gradient field along with the FFL (Fig. 1). The transverse gradient coils could be moved along the FFL direction, such that the relative position of the gradient with respect to the imaging object changed after each excitation cycle. The movement of the center of the gradient coils is expressed as follows:

$$\Delta x = FOV/(N - 1), \quad (1)$$

where  $N$  denotes the number of encoding steps ( $N > 1$ ). This mechanical movement can be replaced via the addition of a homogeneous pulsed excitation field with different amplitudes at each pulse cycle. The excitation field on the FFL generated by the gradient coils after each movement is expressed as follows:

$$\mathbf{H}_G(\mathbf{r}, t) = G_x(t) \cdot \left( x + k\Delta x - \frac{FOV}{2} \right) \hat{\mathbf{i}}, k = 0, 1, \dots, N - 1. \quad (2)$$

The gradient amplitude has the following pulsed waveform to excite magnetic nanoparticles:

$$G_x(t) = -G_0 \sum_{m=0}^{M-1} (-1)^m \Pi(2ft - m), \quad (3)$$

where  $G_0$  is the gradient excitation field strength,  $f$  is the excitation field frequency, and  $\Pi$  is the rectangular function [20]. The pulsed gradient amplitude  $G_0$  was fixed throughout the scanning process, and  $M$  is sufficiently large to cover the complete scan.

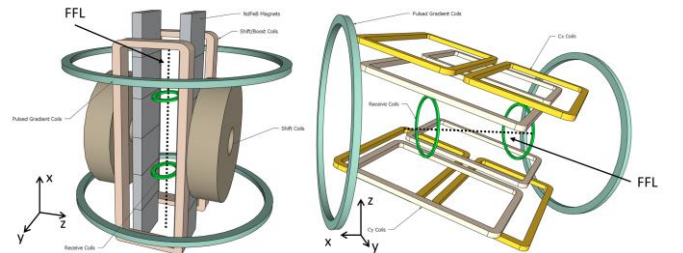


Fig. 1. Diagram of two FFL-based MPI systems with pulsed gradient excitation. Left: Permanent NdFeB magnets were used to generate a vertical FFL [12]. Vertical movement of pulsed gradient coils was used for 1D relaxation encoding. Translations of FFL were controlled by shift coils for 2D and three-dimensional (3D) scans. Right: Open-sided MPI system with electronically rotating FFL [14]. MRI transverse gradient coils generated pulsed inhomogeneous excitation field along with the shifting or rotating FFL. Receiver coils can collect relaxation-induced decay signals from magnetic nanoparticles for high-resolution imaging.

### B. Relaxation-induced Decay Signal

Receiver coils were used to collect the  $x$ -direction magnetization changes of magnetic nanoparticles on the FFL. The receiver coils can be any type of radiofrequency receiver coils, such as full solenoid coils, Helmholtz coils, surface coils, or phased array coils [26].

Under the assumption that the simplest case is that of a 1D straight-line phantom along with the FFL, the magnetic particle

distribution along the  $x$ -axis is  $c(x)$ . The voltage signal induced in the receiver coils can be expressed as follows:

$$u(t) = - \int_{-FOV/2}^{FOV/2} \mu_0 \left( \frac{d\tilde{M}(x,t)}{dt} * R(t) \right) s(x) c(x) dx, \quad (4)$$

where  $\tilde{M}(x,t)$  is the magnetization of magnetic nanoparticles excited by a pulsed gradient field,  $\mu_0$  denotes the permeability of free space, and  $s(x)$  is the sensitivity of the receiver coils. Meanwhile,  $R(t)$  is the Debye relaxation kernel of magnetic nanoparticles, defined as follows:

$$R(t) = \frac{1}{\tau} \exp\left(-\frac{t}{\tau}\right) S(t), \quad (5)$$

where  $S(t)$  is the Heaviside step function, and  $\tau$  is the relaxation time constant. Without relaxation, the voltage signal is considered to be an adiabatic signal and is zero during the flat portion of the pulsed excitation (Fig. 2 Left). The relaxation effects of the nanoparticles induce a magnetization lag and non-zero decay signal during the flat portion of the pulsed excitation [20]. The area under the curve of the decay signal during the flat portion of the pulsed excitation ( $AUC_{flat}$ ) is defined as follows:

$$AUC_{flat} = \int_{flat\_portion} u(t) dt. \quad (6)$$

It should be noted that  $AUC_{flat}$  has a non-linear relationship with the excitation field amplitude, thus confirming the feasibility of the MRI transverse gradient field as an inhomogeneous excitation field for relaxation-based spatial encoding (Fig. 2 Right).

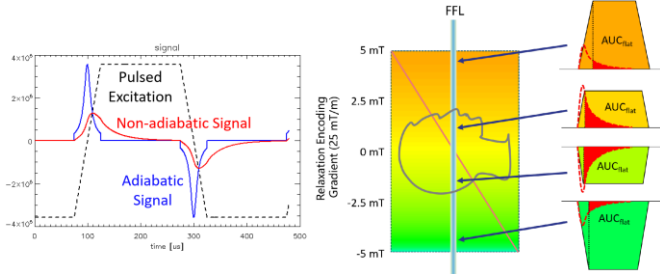


Fig. 2. Left: Adiabatic signal was calculated using Langevin function under pulsed excitation. Signal became zero during flat portion of pulsed excitation. Non-adiabatic signal was calculated using Debye relaxation model and was non-zero during the flat portion because of relaxation effects. Right: Relaxation-induced decay signal  $AUC$  exhibited a non-linear relationship with the pulsed excitation field amplitude. Pulsed gradient field excitation provided 1D spatial encoding on an FFL.

### C. Relaxation Encoding and Image Reconstruction

There are  $N$  1D encoding steps corresponding to  $N$  pulsed gradient profiles on the FFL. For the  $i$ th step, the decay signal  $AUC_{flat,i}$  is as follows:

$$AUC_{flat,i} = \sum_{j=0}^{N-1} AUC_{RX,i}(x_j) c(x_j). \quad (7)$$

The total relaxation-induced decay signal  $AUC$  during the flat portion of a pulsed excitation is calculated based on a single particle's  $AUC_{flat}$ , receiver coil sensitivity, and particle concentration at every voxel on the FFL. Based on the non-linear relationship between the decay signal  $AUC_{flat}$  and the excitation field amplitude, we obtain  $N$  independent linear equations. We can use the matrix to represent these equations as follows:

$$AUC_{RX} \mathbf{C} = AUC_{flat}, \quad (8)$$

where  $\mathbf{C} = [c(x_0), c(x_1), \dots, c(x_{N-1})]$  is the particle

concentration vector along the FFL, and  $AUC_{flat} = [AUC_{flat,0}, AUC_{flat,1}, \dots, AUC_{flat,N-1}]$  is the decay signal vector. The system matrix is expressed as

$$AUC_{RX} = \begin{bmatrix} AUC_{RX,0}(x_0) & \dots & AUC_{RX,0}(x_{N-1}) \\ \vdots & \ddots & \vdots \\ AUC_{RX,N-1}(x_0) & \dots & AUC_{RX,N-1}(x_{N-1}) \end{bmatrix} \quad (9)$$

The system matrix  $AUC_{RX}$  is determined by the gradient excitation profiles and the receiver coil sensitivity map. Based on the measured decay signal  $AUC_{flat}$  vector and calibrated system matrix  $AUC_{RX}$ , we can solve these equations and obtain the solutions to  $\mathbf{C}$ , the 1D nanoparticle concentration vector on the FFL. Direct matrix inversion and iterative reconstruction methods [27] can be used to determine the solutions [28].

In a raster scan, during the parallel movement of the FFL with respect to the object, the gradient excitation continues to move along with the FFL. Combining 1D FFL pixels at different raster locations forms a 2D cross-sectional image. Similarly, the parallel movement of the FFL in the 3<sup>rd</sup> direction generates multiple slices for the 3D volumetric scan.

## III. MATERIALS AND METHODS

In this section, we describe the simulation process using a gradient-pulsed excitation field for the 1D FFL spatial encoding and 2D imaging. A 1D bar pattern phantom, 2D Shepp–Logan phantom, and brain vessel maps were used to evaluate the reconstructed-image quality.

### A. Simulation Software

The simulation was performed using in-house developed software based on the Interactive Data Language (IDL, Exelis Visual Information Solutions, Boulder, CO, USA).

### B. Magnetic Nanoparticles

We simulated a set of magnetic nanoparticles with particle sizes ranging within 20–38 nm. Linear interpolation of the relaxation time measurement [20] was performed to estimate the relaxation time at a specific pulsed-excitation field amplitude (Fig. 3 Left). Langevin function was used to estimate the adiabatic signal, from which the non-adiabatic signal was calculated using the Debye relaxation model.

### C. Gradient Excitation Profiles and System Matrix

Based on the magnetostimulation and SAR analysis in [20], we fixed the pulsed gradient amplitude at 25 mT/m based on an assumption of an FOV of 0.2 m. We set the pulsed excitation frequency to be 2.5 kHz. Each cycle, which had a duration of 400  $\mu$ s, included one positive square wave and one negative square wave with the same shape and duration. The flat portion is defined as the percentage of the gradient field hold time during the entire excitation period. Pulsed excitation fields with different flat portions (50% to 95%) were used to simulate the encoding process (Fig. 3 Right) and to calculate the relaxation-induced decay signal.

Based on  $N$  gradient profiles, a system matrix was constructed based on the calibration curve between the non-adiabatic decay signal ( $AUC_{flat}$ ) and pulsed excitation field



amplitude. Singular value decomposition (SVD) was applied on the system matrix [29] to determine the solution of Equation 8 for 1D image reconstruction [30]. The rates at which the singular values fall off and the extent to which noise would be the limiting factor were evaluated [31].

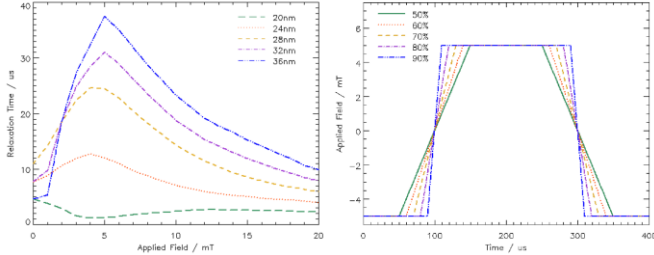


Fig. 3. Relaxation times of differently sized nanoparticles (left) and pulsed square wave excitation fields with different flat portions (right).

#### D. Phantoms and Quality Assessment

A 1D bar pattern phantom with an FOV of 0.2 m was artificially designed with 256 or 512 pixels (Fig. 4 Left). The phantoms included line pairs (lps) with different widths (1–10 black and white pixels). The full width at half maximum (FWHM) based on the modulation transfer function was calculated to evaluate the resolutions of the reconstructed images.

For an FFL-based raster scan and image reconstruction simulation, the 2D Shepp–Logan phantom (Fig. 4 Left) and the segmented brain vessel maps were included in this study. Transverse-direction maximum intensity projection images were generated from nine brain time-of-flight (TOF)-MRA datasets (Fig. 4 Right). The correlation coefficient and root mean square error (RMSE) between the original and reconstructed images were used for image quality assessment.

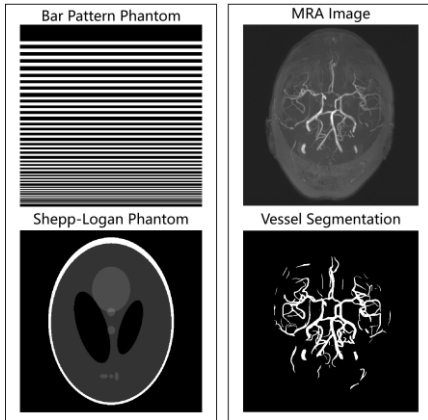


Fig. 4. Left: 1D bar pattern phantom as a row from the 2D bar pattern phantom image and a 2D Shepp–Logan phantom were used to evaluate image quality. Right: Brain vessel maps were generated from brain TOF-MRA images.

#### E. Pulsed Excitation Experiment

To evaluate the relaxation-induced decay signals, Perimag (Micromod GmbH, Germany) coated with dextran (plain surface), and Synomag-D (Micromod GmbH, Germany) coated with dextran (surface, PEG 25,000 OMe) were excited with pulsed excitation [32]. The concentrations of the Perimag and Synomag-D samples were 0.5 mg Fe/ml.

The samples were placed in an arbitrary waveform relaxometer (AWR) developed in-house and excited by a homogeneous pulsed waveform field. The excitation frequency was 2 kHz, and the flat portion was 90%. The field amplitudes were 2.5, 5, and 7.5 mT. The signal-sampling frequency was 10<sup>3</sup> kHz.

The decay signal AUC during the flat portion was calculated to obtain  $AUC_{flat}$ . The evaluated relationship between  $AUC_{flat}$  and the excitation field amplitude could be used as a calibration curve for the system matrix determination (Fig. 5).

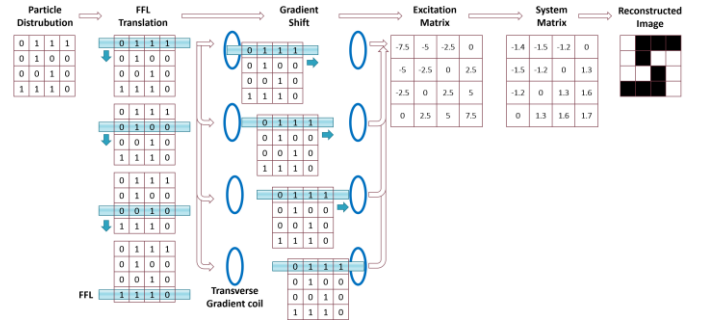


Fig. 5. Pulsed gradient excitation and encoding process for 2D imaging. 1D image on FFL can be reconstructed based on system matrix. 2D imaging requires translation of FFL and gradient excitation field.

## IV. RESULTS

The AUC of the relaxation-induced decay signal within the flat portion exhibited a non-linear relationship with the pulsed excitation field amplitude, which is an odd function and zero when the field amplitude is zero. As the pulsed excitation field amplitude increased from zero,  $AUC_{flat}$  increased and exhibited a peak at 2–7 mT. The  $AUC_{flat}$  then decreased as the field amplitude further increased. The peak  $AUC_{flat}$  increased proportionally to the particle size and the flat portion of the pulsed excitation (Fig. 6).

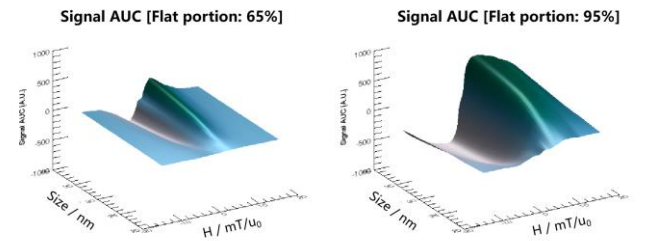


Fig. 6. Signal  $AUC_{flat}$  vs. pulsed excitation fields with different flat portions (65% and 95%) and particle sizes (20 to 38 nm).

The FWHMs of the reconstructed 1D bar phantom images decreased with an increase in the number of encoding steps. A greater flat portion for nanoparticles with fixed diameters allows for a smaller FWHM with a higher spatial resolution (Fig. 7). There were larger nanoparticles and a greater flat portion in the 1D bar phantom images with a higher resolution.

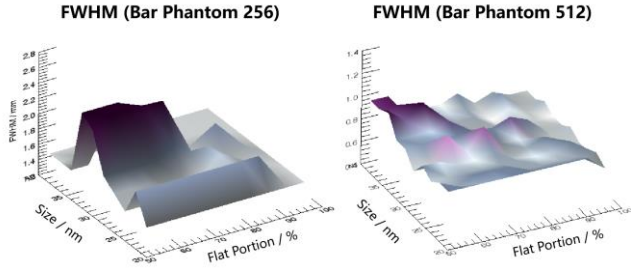


Fig. 7. FWHM measurements using 256 (left) and 512 (right) encoding steps. Particles with different sizes and pulsed excitation with different flat portions were used to simulate the encoding process and 1D bar pattern phantom reconstruction.

Based on the SVD analysis of the system matrix, the singular values quickly fell off. A discontinuity appeared at singular value component index 220, out of 256 components (Fig. 8). At this point, noise may be the limiting factor. More singular value components are still required to reconstruct the 1D phantom with the finest bar pattern.

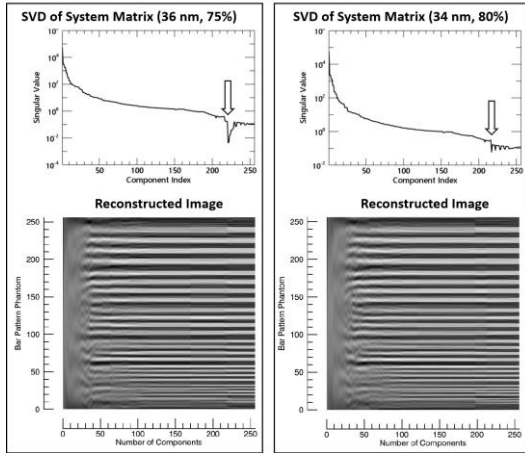


Fig. 8. Singular values rapidly fell off from SVD of system matrix. Discontinuity is observed at component index 220 (hollow arrows). Reconstructed 1D bar pattern phantom image exhibited a higher resolution using a greater number of singular value components.

The reconstructed brain vessel maps revealed stronger correlations and lower RMSEs for larger nanoparticles and a greater flat portion in the pulsed excitation (Fig. 9).

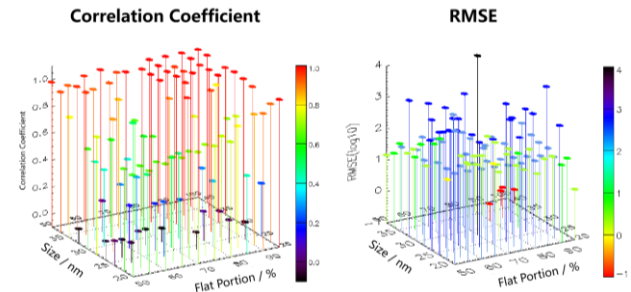


Fig. 9. Average correlation coefficients (left) and median RMSEs (right) of reconstructed brain vessel maps from nine datasets with respect to different flat portions in pulsed excitation and different particle sizes.

The reconstructed 2D Shepp–Logan phantom and brain vessel maps contained less line-by-line inhomogeneity and lower SNR with greater flat portions in pulsed excitation (Fig.

10).

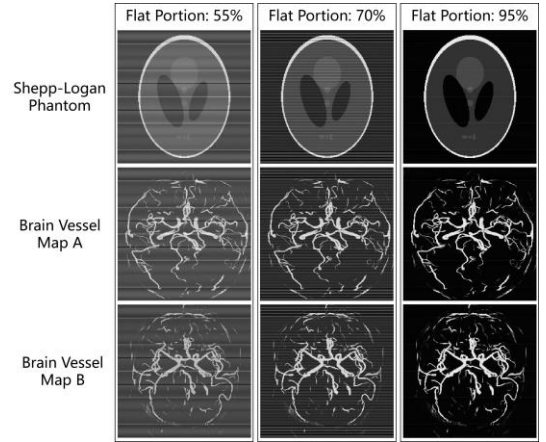


Fig. 10. Reconstructed 2D Shepp–Logan phantom and brain vessel maps using different flat portions in pulsed excitation and particle size of 38 nm.

Magnetic nanoparticles in AWR excited by pulsed waveform fields exhibited non-zero relaxation-induced decay signals during the flat portion. Synomag-D yielded a two-fold signal amplitude compared to that of Perimag. The decay signal AUC ( $AUC_{flat}$ ) exhibited a non-linear relationship with the field amplitude. The values of  $AUC_{flat}$  exhibited their peaks at 2–5 mT for both Perimag and Synomag-D (Fig. 11).

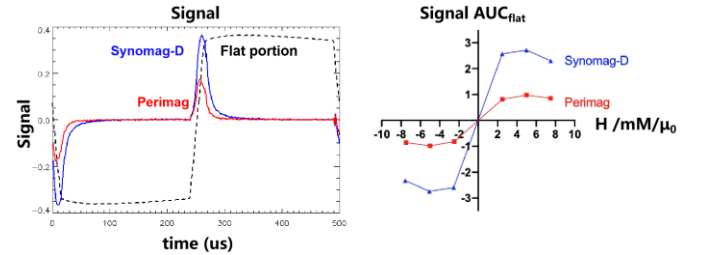


Fig. 11. Left: Perimag and Synomag-D samples exhibited non-zero signals during flat portion of pulsed excitation (dashed line). Synomag-D (blue line) showed a much greater signal than that of Perimag (red line). Right: Signal integral  $AUC_{flat}$  of Perimag and Synomag-D exhibited nonlinear relationship with respect to excitation field amplitude. Peaks of  $AUC_{flat}$  were at approximately 2 to 5 mT for both Perimag (red line) and Synomag-D (blue line).

## V. DISCUSSIONS

### A. Inhomogeneous Excitation for Spatial Encoding

We demonstrated the feasibility of gradient-based excitation for signal encoding and image reconstruction. The relaxation-induced decay signal depends on the pulsed excitation-field amplitude [20]. This method is referred to as ‘relaxation encoding’ and is considered complementary to MRI ‘frequency encoding’ and ‘phase encoding’ [33]. Neither frequency encoding nor phase encoding applies to MPI, given that magnetic nanoparticles do not exhibit nuclear magnetization or precession motion properties. However, the idea of using a pulsed gradient field to perform spatial encoding can be applied to MPI for high-resolution imaging.

In theory, the underlying principle of this study is the

excitation of magnetic nanoparticles using an inhomogeneous magnetic field, such that particles at different locations generate a specific signal. A general inhomogeneous magnetization field was generated using excitation coil arrays [34]. The sequential activation of distinct inhomogeneous fields resulted in a complete scan of an imaging object [35]. General inhomogeneous excitation fields have been used in superconducting quantum interference devices (SQUIDs) to detect magnetic nanoparticles in biological tissues within the picotesla range [36].

This paper proposes the use of a magnetic gradient field for inhomogeneous excitation instead of using excitation coil arrays. For comparison, excitation coil arrays are composed of multiple small coils with limited penetration depths. Meanwhile, the center of the imaging object may exhibit a high noise and low SNR [37]. Isosurfaces with the same field amplitude generated by coil arrays will then tend to be irregular and pose difficulties in spatial decoupling for cross-sectional image reconstruction [35]. On the other hand, linear inhomogeneous gradient excitation fields have been extensively used in MRI for spatial encoding [38]. Through a combination of the gradient field with the FFL in MPI, the nanoparticles on the FFL are exposed to a linearly varying excitation field. Thus, the gradient-based excitation in the pulsed waveform on the FFL does not have a penetration depth limit or spatial decoupling problem.

### B. Integration into FFL-based MPI System

The pulsed-gradient excitation proposed in this work can be integrated into any FFL-based MPI system [39]. One method of generating an FFL is through the use of two NdFeB permanent-magnet sections [12] or a quadrupole magnet [40]. An FFL can also be generated and rotated by Maxwell coil pairs located at equidistant angles on a circle [41]. A third method to generate and rotate an FFL involves using split coils side-by-side with alternating current directions [14]. Moreover, a static FFL can be generated using Halbach rings [42]. A Helmholtz coil pair can always be used to match these FFL designs to generate a pulsed gradient field in the FFL direction for excitation and spatial encoding. High-resolution 1D images, which record part of the FFL rotation or translation steps on these scanners, can then be reconstructed on the FFLs.

In this study, it is crucial to choose MRI transverse gradients using Helmholtz coils as the pulsed gradient excitation fields. In FFP-based MPI, the superimposed effect of the pulsed excitation and selection fields would cause the FFP to jump between two points in space. The effect would cause all nanoparticles lying in between to react simultaneously [20], reducing the image resolution. Therefore, a low excitation field amplitude would be required to minimize the jumping distance between two points. Another solution is to make the excitation field direction perpendicular to the FFP shifting and rotation direction, such that the in-plane resolution becomes insensitive to pulsed excitation [43]. However, this solution may increase slice thickness because the FFP jumping direction is perpendicular to the imaging plane. In FFL-based MPI, the selection field direction is always perpendicular to the FFL

direction [13]. The magnetic field direction and gradient direction of Helmholtz coils are the same as the FFL direction [44], such that the pulsed excitation field on the FFL does not cause the jumping of the FFL. Therefore, there is no image blurring or limitation on the excitation field amplitude [43].

### C. Spatial Resolution and Scan Time

In MPI, both the nanoparticle properties and gradient field strength of the selection field determine the image spatial resolution. The spatial resolution improves with nanoparticles exhibiting a steeper slope on the magnetization–excitation field curve [45]. Superferromagnetic iron oxide nanoparticle chains (SFMIOs) with an ideal step-like magnetization response enable order-of-magnitude resolution in MPI [46]. With this type of nanoparticles, the image resolution remains limited by the size of the FFR, which is inversely proportional to the gradient strength of the selection field. Thus, the FFR cannot be excessively small. However, the size of the FFR is restricted by the limitations of existing gradient coil hardware, which hinder the clinical translation of MPI.

The spatial resolution of MPI based on the relaxation encoding gradient is determined by the number of encoding steps. The pixel size can be calculated as FOV divided by the number of encoding steps ( $FOV/N$ ). A greater number of encoding steps can generate images with a higher spatial resolution. Herein, we set the FOV as 0.2 m to simulate a human head scan. The pixel size could be 1.56 mm for 128 encoding steps, 0.78 for 256 encoding steps, and 0.39 for 512 encoding steps. FWHM measurement on the 1D bar pattern phantom revealed that 512 encoding steps resulted in reconstructed images that had a significantly greater resolution than that produced using 256 encoding steps.

The scan time is proportional to the number of encoding steps. During each pulsed excitation period, only two encoding gradients can be applied, such that only two data points (i.e. relaxation-induced decay signal AUC values) can be acquired. A possible solution to this problem involves increasing the excitation frequency [43], shortening the flat portion, and increasing the slew rate of the gradient [47].

We may accelerate the scan by analyzing the decay signal using inverse Laplace transform. In this study, we considered only the integral of the relaxation-induced decay signal ( $AUC_{flat}$ ) during the flat portion of the pulsed excitation. In fact, each location on the FFL has a unique excitation field strength, and thus has a unique relaxation time component. The inverse Laplace transform can convert the relaxation signal into a continuous distribution of relaxation time components [48]. Theoretically, the inverse Laplace transform of the decay signal from a half pulse cycle can generate a 1D image of the FFL, which may require further investigation.

One limitation of this study is as follows: only the image spatial resolution along the FFL direction can be dramatically improved using the gradient-based relaxation encoding method. In particular, 2D and 3D images can be acquired via the translation of FFL. However, the spatial resolution along the translation direction is limited by the width of the FFL. A solution to this problem involves repeating the scan, but with



switches in the FFL direction and FFL shifting direction.

#### D. SNR and Pulsed Waveform

The SNR in this relaxation-encoding method is closely related to the transmit slew rate of the pulsed waveform. For particles whose relaxation times are faster than the rise/fall time of the pulse, there might be little to no signal that can be integrated during the flat portion. A two-step relaxation process of colloidal magnetic nanoclusters under pulsed fields with 10 mT was reported by Trisnanto et al. [49], in which the magnetization is described by a bi-exponential decay function. The Néel relaxation time was approximately several microseconds, whereas the Brownian relaxation time was approximately 20–100  $\mu$ s. In this simulation, the rise/fall time is between 5 and 100  $\mu$ s, during which only partial magnetization is recovered. The continuously recovering magnetization in the flat portion can generate non-zero signals for measurement. For pulses with a greater flat portion and a shorter rise/fall time, there might be a greater signal during the flat portion due to a greater amount of recovering magnetization. The simulation results revealed that larger nanoparticles and a greater flat portion of pulsed excitation generate a 1D bar phantom image with a smaller FWHM, and 2D images with a greater correlation coefficient.

Pulsed excitation frequency and Debye relaxation time are crucial to the decay signal analysis of pulsed excitation. If the frequency is excessively high or the Debye relaxation time is excessively long, the signal may not decay to zero by the end of the flat portion, which indicates that the magnetization is not fully recovered. The partially recovered magnetization can result in a decreased magnetization during the rise/fall time of the following pulse. The continuously decreasing magnetization induces gradual decreases in the signal and AUC during the flat portion [20], which would cause system matrix-based image reconstruction to become impossible. In this study, both the Perimag and Synomag-D samples exhibited zero signals at the end of the flat portion under a 2 kHz excitation (Fig. 11), which can guarantee fully recovered magnetization at the beginning of the next pulsed excitation.

There may be SNR degradation due to the ill-posed inverse problem about system matrix-based image reconstruction. The differences in the relaxations and  $AUC_{flat}$  as functions of excitation field amplitude might be minor, suggesting that the inverse problem is not well conditioned. This could be a major problem when our method is implemented in practice. Based on the SVD analysis of the system matrix [29], a discontinuity appeared at a singular value component index beyond 86% of the total components, which might be the limiting factor and affects the reconstruction of the finest bar patterns (Fig. 8). Based on our experiment on the relaxometer, the magnetic nanoparticles exhibited strong SNR at excitation field amplitudes less than 10 mT at a concentration of 0.5 mg Fe/ml (Fig. 11). SNR degradation at low concentrations needs to be evaluated in future studies.

Many technique factors may affect the relationship between the relaxation time and excitation field amplitude. Feedthrough spikes of pulsed MPI and slew limitations can significantly

enhance the decay signal, resulting in the overestimation of AUC and relaxation times [20]. Spectrum analysis of the decay signal based on inverse Laplace transform [48] or multi-exponential relaxation times estimation [50] may be performed to identify the short relaxation components from feedthrough effects and slew limitations. Through the removal of external short relaxation components, accurate estimations of AUC and relaxation time become possible.

Our work combines pulsed gradient excitation and FFL-based MPI for high-resolution imaging. Because the number of nanoparticles on an FFL is greater than that in an FFP [11], FFL-based MPI scanners exhibit higher sensitivity than those of FFP-based MPI scanners and are suitable for large imaging volumes, such as human in vivo imaging [13].

A receiver coil with high sensitivity is crucial for collecting strong signals to achieve high SNR [51]. Because magnetic nanoparticles do not exhibit precession motion with Larmor frequency, there are only magnetization changes along the pulsed gradient excitation field direction. Thus, the receiver coil shape should be designed to efficiently collect magnetization changes [3] and be able to fit in the scanner and patient bed [40].

#### E. Bio-safety Concerns

Pulsed excitation with low amplitude can provide a strong relaxation-induced decay signals for 1D image reconstruction. Low-amplitude pulsed excitations do not lead to bio-safety problems [20]. On the other hand, although high-amplitude pulsed excitation fields have been used to improve image quality [43], the decay signal does not always increase with a greater excitation field amplitude. The experimental data showed that the peaks of  $AUC_{flat}$  were at approximately 2 to 5 mT for both Perimag and Synomag-D. The optimal field amplitude that generates the strongest decay signal should be selected to excite nanoparticles such that spatial encoding is accomplished without any bio-safety problems.

The gradient-based pulsed excitation method for relaxation encoding applies to both small animal and human in vivo imaging. For clinical translation, we used the human brain as a template to set the FOV, gradient amplitude, and phantom images for the simulation. These parameters and hardware need to be adjusted and optimized for small animal and human in-vivo imaging.

## VI. CONCLUSION

In this study, MRI transverse gradient in a pulsed waveform was applied to FFL-based MPI to excite magnetic nanoparticles and generate a relaxation-induced decay signal. Through alignment of the gradient direction with the FFL and the excitation of nanoparticles with many gradient profiles, a high-resolution 1D image was reconstructed on the FFL. The simulation results confirmed the feasibility of MPI pulsed gradient excitation and relaxation encoding for spatially resolved magnetic nanoparticle measurements on the FFL. A relaxation-encoding design with bio-safe pulsed gradient excitation can overcome the difficulty of clinical scaling hardware and facilitate high-resolution human in vivo imaging.

## REFERENCES

- [1] B. Gleich, and J. Weizenecker, "Tomographic imaging using the nonlinear response of magnetic particles," *Nature*, vol. 435, no. 7046, pp. 1214-1217, Jun. 2005.
- [2] A. P. Khandhar, P. Keselman, S. J. Kemp *et al.*, "Evaluation of PEG-coated iron oxide nanoparticles as blood pool tracers for preclinical magnetic particle imaging," *Nanoscale*, vol. 9, no. 3, pp. 1299-1306, Jan. 2017.
- [3] M. Graeser, P. Ludewig, P. Szwargulski *et al.*, "Design of a head coil for high resolution mouse brain perfusion imaging using magnetic particle imaging," *Phys. Med. Biol.*, vol. 65, no. 23, pp. 235007, Dec. 2020.
- [4] C. Z. Cooley, J. B. Mandeville, E. E. Mason *et al.*, "Rodent Cerebral Blood Volume (CBV) changes during hypercapnia observed using Magnetic Particle Imaging (MPI) detection," *NeuroImage*, vol. 178, pp. 713-720, Sep. 2018.
- [5] T. Y. Tang, S. P. S. Howarth, S. R. Miller *et al.*, "Comparison of the inflammatory burden of truly asymptomatic carotid atheroma with atherosclerotic plaques contralateral to symptomatic carotid stenosis: an ultra small superparamagnetic iron oxide enhanced magnetic resonance study," *J. Neurol. Neurosurg. Psychiatry*, vol. 78, no. 12, pp. 1337. 2007.
- [6] O. C. Sehl, and P. J. Foster, "The sensitivity of magnetic particle imaging and fluorine-19 magnetic resonance imaging for cell tracking," *Sci. Rep.*, vol. 11, no. 1, pp. 22198, Nov 12. 2021.
- [7] A. Rivera-Rodriguez, L. B. Hoang-Minh, A. Chiu-Lam *et al.*, "Tracking adoptive T cell immunotherapy using magnetic particle imaging," *Nanotheranostics*, vol. 5, no. 4, pp. 431-444. 2021.
- [8] J. Wells, S. Twamley, A. Sekar *et al.*, "Lissajous scanning magnetic particle imaging as a multifunctional platform for magnetic hyperthermia therapy," *Nanoscale*, vol. 12, no. 35, pp. 18342-18355, Sep 21. 2020.
- [9] M. Graeser, F. Thieben, P. Szwargulski *et al.*, "Human-sized magnetic particle imaging for brain applications," *Nat. Commun.*, vol. 10, no. 1, pp. 1936, Apr. 2019.
- [10] J. Weizenecker, B. Gleich, and J. Borgert, "Magnetic particle imaging using a field free line," *J. Phys. D: Appl. Phys.*, vol. 41, no. 10, pp. 105009, May. 2008.
- [11] K. Bente, M. Weber, M. Graeser *et al.*, "Electronic field free line rotation and relaxation deconvolution in magnetic particle imaging," *IEEE Trans Med Imag.*, vol. 34, no. 2, pp. 644-651, Feb. 2015.
- [12] J. J. Konkle, P. W. Goodwill, O. M. Carrasco-Zevallos *et al.*, "Projection reconstruction magnetic particle imaging," *IEEE Trans. Med. Imag.*, vol. 32, no. 2, pp. 338-347, Feb. 2013.
- [13] C. B. Top, and A. Güngör, "Tomographic Field Free Line Magnetic Particle Imaging With an Open-Sided Scanner Configuration," *IEEE Trans. Med. Imag.*, vol. 39, no. 12, pp. 4164-4173. 2020.
- [14] C. B. Top, S. Ilbey, and H. E. Güven, "Electronically rotated and translated field-free line generation for open bore magnetic particle imaging," *Med. Phys.*, vol. 44, no. 12, pp. 6225-6238, Dec. 2017.
- [15] K. Murase, "Simultaneous correction of sensitivity and spatial resolution in projection-based magnetic particle imaging," *Med. Phys.*, vol. 47, no. 4, pp. 1845-1859, Apr. 2020.
- [16] C. B. Top, A. Gungor, S. Ilbey *et al.*, "Trajectory analysis for field free line magnetic particle imaging," *Med. Phys.*, vol. 46, no. 4, pp. 1592-1607, Apr. 2019.
- [17] J. Pagan, C. McDonough, T. Vo *et al.*, "Single-Sided Magnetic Particle Imaging Device with Field-Free-Line Geometry for in-vivo Imaging Applications," *IEEE Trans. Magn.*, vol. 57, no. 2, Feb. 2021.
- [18] N. Panagiotopoulos, R. L. Duschka, M. Ahlborg *et al.*, "Magnetic particle imaging: current developments and future directions," *Int. J. Nanomedicine*, vol. 10, pp. 3097-3114. 2015.
- [19] Z. W. Tay, D. W. Hensley, P. Chandrasekharan *et al.*, "Optimization of Drive Parameters for Resolution, Sensitivity and Safety in Magnetic Particle Imaging," *IEEE Trans. Med. Imag.*, vol. 39, no. 5, pp. 1724-1734, May. 2020.
- [20] Z. W. Tay, D. Hensley, J. Ma *et al.*, "Pulsed Excitation in Magnetic Particle Imaging," *IEEE Trans. Med. Imag.*, vol. 38, no. 10, pp. 2389-2399, Oct. 2019.
- [21] L. R. Croft, P. W. Goodwill, J. J. Konkle *et al.*, "Low drive field amplitude for improved image resolution in magnetic particle imaging," *Med. Phys.*, vol. 43, no. 1, pp. 424-435. 2016.
- [22] Z. W. Tay, D. W. Hensley, E. C. Vreeland *et al.*, "The Relaxation Wall: Experimental Limits to Improving MPI Spatial Resolution by Increasing Nanoparticle Core size," *Biomed. Phys. Eng. Express*, vol. 3, no. 3, pp. 035003, Jun. 2017.
- [23] P. Mansfield, and A. A. Maudsley, "Medical imaging by NMR," *Br. J. Radiol.*, vol. 50, no. 591, pp. 188-194, Mar. 1977.
- [24] P. C. Lauterbur, "Image Formation by Induced Local Interactions: Examples Employing Nuclear Magnetic Resonance," *Nature*, vol. 242, no. 5394, pp. 190-191, Mar. 1973.
- [25] R. J. Deissler, Y. Wu, and M. A. Martens, "Dependence of Brownian and Neel relaxation times on magnetic field strength," *Med. Phys.*, vol. 41, no. 1, pp. 012301, Jan. 2014.
- [26] F. D. Doty, G. Entzminger, J. Kulkarni *et al.*, "Radio frequency coil technology for small-animal MRI," *NMR Biomed.*, vol. 20, no. 3, pp. 304-325, May. 2007.
- [27] E. Pouget, and V. Dedieu, "Impact of iterative reconstruction algorithms on the applicability of Fourier-based detectability index for x-ray CT imaging," *Med. Phys.*, vol. 48, no. 8, pp. 4229-4241, Aug. 2021.
- [28] X. Chen, Z. Jiang, X. Han *et al.*, "The Reconstruction of Magnetic Particle Imaging: Current Approaches Based on the System Matrix," *Diagnostics (Basel)*, vol. 11, no. 5, Apr 26. 2021.
- [29] G. Landi, F. Zama, and V. Bortolotti, "A New Hybrid Inversion Method for 2D Nuclear Magnetic Resonance Combining TSVD and Tikhonov Regularization," *J. Imag.*, vol. 7, no. 2. 2021.
- [30] W. Yang, J.-Y. Hong, J.-Y. Kim *et al.*, "A Novel Singular Value Decomposition-Based Denoising Method in 4-Dimensional Computed Tomography of the Brain in Stroke Patients with Statistical Evaluation," *Sensors*, vol. 20, no. 11. 2020.
- [31] E. R. Hill, W. Xia, M. J. Clarkson *et al.*, "Identification and removal of laser-induced noise in photoacoustic imaging using singular value decomposition," *Biomed. Opt. Express*, vol. 8, no. 1, pp. 68-77, Jan. 2017.
- [32] M. İrfan, N. Dogan, T. Sapmaz *et al.*, "Development of MPI relaxometer for characterization of superparamagnetic nanoparticles," *J. Magn. Magn. Mater.*, vol. 536, pp. 168082, Oct. 2021.
- [33] T. Luo, D. C. Noll, J. A. Fessler *et al.*, "Joint Design of RF and Gradient Waveforms via Auto-differentiation for 3D Tailored Excitation in MRI," *IEEE Trans. Med. Imag.*, vol. 40, no. 12, pp. 3305-3314, Dec. 2021.
- [34] D. Baumgarten, F. Braune, E. Supriyanto *et al.*, "Plane-wise sensitivity based inhomogeneous excitation fields for magnetorelaxometry imaging of magnetic nanoparticles," *J. Magn. Magn. Mater.*, vol. 380, pp. 255-260, Apr. 2015.
- [35] M. Liebl, U. Steinhoff, F. Wiekhorst *et al.*, "Quantitative imaging of magnetic nanoparticles by magnetorelaxometry with multiple excitation coils," *Phys. Med. Biol.*, vol. 59, no. 21, pp. 6607-6620, Oct. 2014.
- [36] U. Steinhoff, M. Liebl, M. Bauer *et al.*, "Spatially Resolved Measurement of Magnetic Nanoparticles Using Inhomogeneous Excitation Fields in the Linear Susceptibility Range (<1mT)," in *Magnetic Particle Imaging*, Berlin, Heidelberg, 2012, pp. 295-300.
- [37] O. Kamal, S. McTavish, F. N. Harder *et al.*, "Noise reduction in diffusion weighted MRI of the pancreas using an L1-regularized iterative SENSE reconstruction," *Magn. Reson. Imaging*, vol. 87, pp. 1-6, Apr. 2022.
- [38] E. Torres, T. Froelich, P. Wang *et al.*, "B1-gradient-based MRI using frequency-modulated Rabi-encoded echoes," *Magn. Reson. Med.*, vol. 87, no. 2, pp. 674-685, Feb. 2022.
- [39] A. Tonyushkin, "Single-Sided Field-Free Line Generator Magnet for Multi-Dimensional Magnetic Particle Imaging," *IEEE Trans. Magn.*, vol. 53, no. 9, pp. 5300506, Sep. 2017.
- [40] S.-M. Choi, J.-C. Jeong, J. Kim *et al.*, "A novel three-dimensional magnetic particle imaging system based on the frequency mixing for the point-of-care diagnostics," *Sci. Rep.*, vol. 10, no. 1, pp. 11833, Jul. 2020.
- [41] T. Knopp, T. F. Sattel, S. Biederer *et al.*, "Field-free line formation in a magnetic field," *J. Phys. A: Math. Theor.*, vol. 43, no. 1, pp. 012002, Dec. 2009.
- [42] P. Vogel, J. Markert, M. A. Rückert *et al.*, "Magnetic Particle Imaging meets Computed Tomography: first simultaneous imaging," *Sci. Rep.*, vol. 9, no. 1, pp. 12627, Sep. 2019.



- [43] F. Mohn, T. Knopp, M. Boberg *et al.*, "System Matrix based Reconstruction for Pulsed Sequences in Magnetic Particle Imaging," *IEEE Trans. Med. Imag.*, pp. 1-1. 2022.
- [44] P. B. Roemer, and B. K. Rutt, "Minimum electric-field gradient coil design: Theoretical limits and practical guidelines," *Magn. Reson. Med.*, vol. 86, no. 1, pp. 569-580. 2021.
- [45] R. Hufschmid, H. Arami, R. M. Ferguson *et al.*, "Synthesis of phase-pure and monodisperse iron oxide nanoparticles by thermal decomposition," *Nanoscale*, vol. 7, no. 25, pp. 11142-11154, Jul. 2015.
- [46] Z. W. Tay, S. Savliwala, D. W. Hensley *et al.*, "Superferromagnetic Nanoparticles Enable Order-of-Magnitude Resolution & Sensitivity Gain in Magnetic Particle Imaging," *Small Methods*, vol. 5, no. 11, pp. e2100796, Nov. 2021.
- [47] T. K. F. Foo, E. T. Tan, M. E. Vermilyea *et al.*, "Highly efficient head-only magnetic field insert gradient coil for achieving simultaneous high gradient amplitude and slew rate at 3.0T (MAGNUS) for brain microstructure imaging," *Magn. Reson. Med.*, vol. 83, no. 6, pp. 2356-2369. 2020.
- [48] P. Berman, O. Levi, Y. Parmet *et al.*, "Laplace inversion of low-resolution NMR relaxometry data using sparse representation methods," *Concepts Magn. Reson.*, vol. 42, no. 3, pp. 72-88, May. 2013.
- [49] S. B. Trisnanto, S. Ota, and Y. Takemura, "Two-step relaxation process of colloidal magnetic nanoclusters under pulsed fields," *Appl. Phys. Express*, vol. 11, no. 7, pp. 075001, Jun. 2018.
- [50] C. E. Hajj, S. Moussaoui, G. Collewet *et al.*, "Multi-Exponential Transverse Relaxation Times Estimation From Magnetic Resonance Images Under Rician Noise and Spatial Regularization," *IEEE Trans. Image Process.*, vol. 29, pp. 6721-6733. 2020.
- [51] J. Jin, E. Weber, Y. Tesiram *et al.*, "Image Reconstruction for a Rotating Radiofrequency Coil (RRFC) Using Self-Calibrated Sensitivity From Radial Sampling," *IEEE Trans. Biomed. Eng.*, vol. 64, no. 2, pp. 274-283, Feb. 2017.